Quantitative first-principles calculations of valence and core excitation spectra of solid C$_{60}$

F. Fossard and G. Hug

ONERA-CNRS, Laboratoire d'Étude des Microstructures, BP 72, F-92322, Châtillon Cedex, France

K. Gilmore

European Synchrotron Radiation Facility (ESRF), BP 220, F-38043 Grenoble, France

J. J. Kas, J. J. Rehr, and F. D. Vila

Department of Physics, University of Washington, Seattle, Washington 98195, USA

E. L. Shirley[*]

Sensor Science Division, National Institute of Standards and Technology (NIST), 100 Bureau Dr. MS 8441, Gaithersburg, Maryland 20899-8441, USA

We present calculated valence and C 1s near-edge excitation spectra of solid C$_{60}$ and experimental results measured with high-resolution electron energy-loss spectroscopy. The near-edge calculations are carried out using three different methods: solution of the Bethe-Salpeter equation (BSE) as implemented in the OCEAN suite (Obtaining Core Excitations with *Ab Initio* methods and the NIST BSE solver), the excited-electron core-hole approach, and the constrained-occupancy method using the Stockholm-Berlin core excitation code, StoBe. The three methods give similar results and are in good agreement with experiment, though the BSE results are the most accurate. The BSE formalism is also used to carry out valence level calculations using the NIST BSE solver. Theoretical results include self-energy corrections to the band gap and bandwidths, lifetime-damping effects, and Debye-Waller effects in the core excitation case. A comparison of spectral features to those observed experimentally illustrates the sensitivity of certain features to computational details, such as self-energy corrections to the band structure and core-hole screening.

I. INTRODUCTION

The highly symmetrical (icosahedral group) C$_{60}$ molecule, as well as other fullerenes and their compounds, including crystalline solid C$_{60}$, have been of interest since the discovery of C$_{60}$ in 1985 and the subsequent ability to produce high-quality, high-purity samples in large quantities [1,2]. Numerous applications for C$_{60}$ and related compounds have since been suggested. Owing to the strong electron-accepting nature of C$_{60}$, polymer-C$_{60}$ blends are routinely proposed as organic photovoltaic devices [3,4]. Various other aspects of C$_{60}$-based materials have been investigated, including their nonlinear optical properties [5], superconductivity [6,7], and potential as hydrogen storage materials [8]. The viability of C$_{60}$-based materials for many proposed applications depends on their electronic and excited-state properties, which are typically probed spectroscopically. Pure molecular C$_{60}$ is a natural testbed for both experimental and theoretical techniques. Here we study excited states and spectra of pure C$_{60}$ to ascertain the current level of accuracy of the various computational methods. To do so, we present measured and calculated results for (i) the valence excitation spectrum of solid C$_{60}$ below 70 eV, capturing most of the valence oscillator strength, and (ii) the C 1s near-edge spectra over a comparable energy range.

The excitation properties of condensed-phase C$_{60}$ are similar to those of molecular C$_{60}$ (free or in solution), which aids interpretation of the former. Thus our excitation spectra

are heavily influenced by the electronic structure of the molecule, whose occupied and unoccupied molecular orbitals (MOs) form bands in the solid. This is most clear near the valence and core excitation thresholds, but is also evident in the contribution of broadened unoccupied electron states at higher energies. Features particular to solid-state spectra give insight into intermolecular interactions.

For the energy ranges considered, it is crucial to treat the excited-state electronic structure using accurate first-principles methods, including excitonic effects and self-energy effects on electronic states. For the intermediate energy range of about 70–280 eV and above 335 eV, multiple-scattering treatments [9] and/or atomic cross-section data can account well for the remainder of the electronic excitation spectrum, while a density functional perturbation theory (DFPT) treatment [10] that accounts for infrared-active vibrational absorption completes the optical spectrum.

In the next section, we discuss the theoretical approaches used to compute the electron energy-loss spectroscopy (EELS) signal. This is followed by a description of the experimental methodology, namely, EELS in a transmission electron microscope. Results are then presented and compared, both to each other and to past work. A summary and concluding remarks are then provided.

II. THEORETICAL METHODS

The C 1s near-edge excitation spectrum was calculated within the Bethe-Salpeter formalism, the excited-electron core-hole density function theory (DFT) method, and with

---

[*]eric.shirley@nist.gov

the StoBe code. In each case, the resulting spectra were corrected by the same set of postprocessing corrections that take into account lifetime broadening, plasmon satellites, and Debye-Waller damping effects. These postprocessing steps followed the main calculations, and we discuss them in turn below. The valence excitation spectra were calculated with the Bethe-Salpeter equation (BSE) and also included lifetime broadening effects.

A. Bethe-Salpeter calculations

We performed core excitation BSE calculations as described by Vinson and co-workers [11,12], who detailed the OCEAN (Obtaining Core Excitations with *Ab Initio* methods and the NIST BSE solver) code. The electronic charge density was found using self-consistent field calculations in the local density approximation (LDA) as described elsewhere [13]. To emphasize transferability, we used a hard Vanderbilt-style norm-conserving pseudopotential [14] with a 40.5-Hartree (81 Rydberg) plane-wave cutoff. We used 800 band states at the zone center and its 14 images in higher Brillouin zones following the optimized-basis-function (OBF) methodology advanced particularly by Prendergast and Louie [15], who followed Shirley [16]. We retained 2000 OBFs (hence, 34 basis functions per atom) to describe 800 bands of Bloch states throughout the Brillouin zone. This completely described electron levels up to about 50 eV above the Fermi level and captured salient oscillator strengths germane to low-momentum-transfer loss spectra. Electronic states were augmented as described by Shirley [17] for purposes of random-phase approximation screening of the core hole according to a real-space scheme [18] and for computing on-site electron core-hole interactions in core excited states.

Screening calculations require a value for ϵ_∞. From DFPT Giannozzi and Baroni [10] reported a polarizability consistent with $\epsilon_\infty = 4.95$, close to the value obtained by us ($\epsilon_\infty = 5.09$). Yagi *et al.* [19] reported a measured value of $\epsilon_\infty = 4.62$, which we have used in this work.

The band gap of C_{60} is found from combined photoelectron spectroscopy (PES) and inverse photoelectron spectroscopy (IPES) to be between 2.3 and 2.6 eV. However, density functional theory [20], when using the LDA to the exchange-correlation functional [21–23], yields a significantly smaller value. Shirley and Louie [24] obtained an LDA band gap of about 1.04 eV, in agreement with Troullier and Martins [25], and showed that this increases to about 2.15 eV using Hedin's GW approximation [26]. The remaining difference from the experimental result could stem partly from surface-induced band bending. The LDA band structure also compresses the "energy scale" within the occupied and unoccupied energy windows. To correct this, compared to the PES and IPES spectra [27–31], we included a 10% enhancement of LDA bandwidths. Such band widening is reminiscent of that in other systems, particularly graphite [32–35]. We note that relative intensities of features in the lower-energy portion of the spectrum are sensitive to such band stretching and the value of ϵ_∞.

Core BSE calculations used $2 \times 2 \times 2$ Brillouin-zone sampling for core-hole screening and $3 \times 3 \times 3$ sampling

to obtain near-edge spectra. The grids were shifted to accelerate convergence. Nearly identical spectra were found using $2 \times 2 \times 2$ Brillouin-zone sampling, such that features changed on a level small compared to the typical level of agreement with experiment. We included 800 bands in the calculation, including the 120 occupied bands, but "occupied" portions of spectra were omitted in the presented results. This allowed for level-repulsion and mixing of occupied and unoccupied states in the presence of the core hole.

Valence BSE calculations were carried out as described by Lawler *et al.* [36] and relied on the same LDA calculations, OBFs, and an input value of ϵ_∞. We included 120 occupied bands and 680 unoccupied bands. Calculations were carried out using $2 \times 2 \times 2$ Brillouin-zone sampling. Results were nearly indistinguishable from those using $1 \times 1 \times 1$ Brillouin-zone sampling. Calculations only included forward-going electron-hole pair states. For comparison, Koval *et al.* [37] presented the loss function calculated by time-dependent DFT.

B. Excited-state core-hole calculations

The core excitation spectrum was also calculated using the final-state, excited-state core-hole (XCH) method of Prendergast and Galli [38]. The necessary final-state DFT calculations were performed with ultrasoft pseudopotentials using the Perdew-Burke-Ernzerhof generalized gradient approximation (PBE-GGA) exchange-correlation functional within the QUANTUM ESPRESSO DFT package [39]. A pseudopotential containing a full core-hole in the $1s$ level was used at the absorbing atomic site and an extra electron was placed at the bottom of the conduction band, representing the excited electron, leaving a charge-neutral excitation. Separate self-consistent field (SCF) and non-self-consistent field (NSCF) calculations were performed as the core-hole pseudopotential was moved to each unique absorbing site. All calculations were performed with $2 \times 2 \times 2$ sampling of the Brillouin zone and 1440 bands for the 240-atom $Pa3$ unit cell. We confirmed both that there is little difference between the C $1s$ near-edge spectra for the 60-atom $Fm3$ unit cell and 240-atom $Pa3$ unit cell (by BSE calculations), and that the ground-state densities of states generated from either norm-conserving LDA or ultrasoft GGA pseudopotentials are quite similar. Screening of the core hole occurs explicitly throughout the full unit cell within the final-state calculation, obviating the need to supply a value of ϵ_∞, contrary to our implementation of the Bethe-Salpeter method. Furthermore, within the final-state approach, mixing of the initial state occupied and unoccupied levels occurs naturally.

C. STOBE calculations

The core excitation spectrum was also calculated using the Slater-transition-potential approach [40] with the StoBe deMon code [41]. These calculations were performed only on an isolated molecule with the structure extracted from the crystal. Two dominant factors that affect the quality of the results are the quality of the Gaussian basis set and the strength of the core-hole potential used. To ensure

converged results over the first 20–25 eV above the edge, we used a fully uncontracted IGLO III basis set [42] for the absorbing atom (where IGLO stands for "individual gauge for localized orbitals"), augmented with 21 s, p, and d diffuse exponents and supplemented with (5,2;5,2) auxiliary basis functions for the computation of the spatial integrals. The nonabsorbing C atoms used (321/311/1) basis sets associated with (3,1:8,0) effective core potentials, and supplemented with (5,2;5,2) auxiliary basis functions. In the transition potential method, the strength of the core hole is controlled by changing the occupation of the core state of interest. An occupation of one half of one electron usually results in good overall excitation energies. Here, however, we find that to account for the large intensity of the first peak relative to the rest of the spectrum, a much stronger core hole is needed. Thus, the results presented in the next section were obtained with a fully unoccupied $1s$ state and shifted in energy to match the first experimental peak. All StoBe simulations used the BP86 gradient-corrected exchange-correlation functional [43].

D. Lifetime-broadening effects and inclusion of satellites

Electron self-energy effects on real parts of band energies were determined following Fister $et\ al.$ [44] but with a 10% enhancement of band-energy separations near the Fermi level. Damping was estimated using the multiple-pole self-energy treatment of Kas $et\ al.$ [45] using the experimental small-**q** (optical) loss function, i.e., $-\mathrm{Im}[1/\epsilon(\mathbf{q} \to 0,\omega)]$, from Yagi $et\ al.$ [19]. The extended x-ray absorption fine structure (EXAFS) Debye-Waller (DW) factor (using Hartree atomic units with $e = 1, \hbar = 1, m_e = 1$) is $\exp(-2k^2\sigma_i^2)$, where $k = [2(E - E_0)]^{1/2}$ is the EXAFS wave number defined relative to the edge energy E_0, and σ_i^2 is the mean-square relative displacement for scattering path i [46]. In C_{60}, the mean-square relative displacement is an approximately linear function of path length [47], so the Debye-Waller factor becomes $\exp(-2k^2\sigma_0^2 R_i/R_0)$, where R_i and R_0 are the half-path length and nearest-neighbor bond length. One can relate this factor to the EXAFS inelastic mean-free-path damping factor, $\exp[-2R_i/\lambda(k)]$ [46], to derive the effective inelastic mean-free path, $\lambda_{\mathrm{DW}}(k) = R_0/(k\sigma_0)^2$. The inelastic mean-free path is related to the imaginary part of the self-energy by $\lambda(k) = k/|\mathrm{Im}\{\Sigma(E - E_0)\}|$ [46]. Hence, the effective self-energy broadening is $|\mathrm{Im}\{\Sigma_{\mathrm{DW}}(E - E_0)\}| = [2(E - E_0)]^{3/2}\sigma_0^2/R_0$. We assumed $\sigma_0^2/R_0 = 0.29\,\mathrm{pm}$ from neutron scattering [47].

For valence calculations, we included self-energy broadening of electron and hole band states [44]. For damping of electron-hole pair states, we averaged over all pair states with band-energy differences within 0.05-eV-wide bins. This defined an effective electron-hole pair damping function $\Sigma_{\mathrm{eh}}''(E)$, which could be interpolated with respect to energy. The valence excitation spectrum was smoothed according to

$$\epsilon_2(E) = \pi^{-1} \int_0^\infty dE' \epsilon_{2,\mathrm{nb}}(E') |\Sigma_{eh}''(E')| / \{(E - E')^2 + [\Sigma_{eh}''(E')]^2\}, \tag{1}$$

where $\epsilon_{2,\mathrm{nb}}(E')$ denotes the imaginary part of the dielectric function output from the valence BSE calculations with no broadening.

III. EXPERIMENTAL METHODS

Electron energy-loss spectroscopy experiments in transmission electron microscopy (TEM) were performed in a Zeiss Libra 200 microscope with a Schottky field-emission gun (FEG) that provided an electron source of high brightness and coherence. A CEOS (Corrected Electron Optical Systems, GmbH, Germany) monochromator improved the energy dispersion. Such a monochromator is purely electrostatic and has the shape of an omega with four deflections. An astigmatic dispersive image of the virtual source was formed in the symmetry plane of the monochromator and filtered with a slit to obtain an 8-meV energy width. Various slit widths can be achieved using a piezoelectric actuator. The beam was subsequently accelerated to a high tension that could be varied between 80 and 200 keV. To minimize sample radiation damage and degraded energy resolution because of voltage fluctuations, an 80-keV operating voltage was selected, despite an increase of the multiple losses in the sample that distort the EELS signal [48]. From the elastic peak FWHM, we estimated the overall energy resolution to be 0.12 eV.

After the sample, the beam passed through an Omega filter that can render real-space images and diffraction patterns. The energy-selection process involves four deflections of about $90°$ obtained with four magnetic sectors. The deflected beam is corrected up to second order with hexapoles and quadrupoles. A slit can be inserted in the symmetry plane of the filter. The filter can be operated in a variety of optical modes, including a simple dispersive mode that allows for the projection of spectra onto the detector. Here the microscope was operated in scanning TEM (STEM) mode, so that an image (or diffraction pattern) was created using a nanoscale probe that was focused and swept across the sample while the beam intensity was recorded as a function of position. The projector optical system was tuned to form a diffraction pattern at the entrance plane of the filter. We recorded spectra with a Gatan Ultrascan charge-coupled device (CCD) camera that had a 2000×2000 pixel array, of which only one 100×2000 portion was used in spectroscopy mode because of the elongated shape of the image. Data were automatically corrected for dark current and nonuniform pixel gain.

Low-loss spectra were recorded with an integration time of 0.2 s, repeated 20 times, and averaged to improve statistics. For core-loss spectra, the integration time was 5 s, and 20 spectra were similarly averaged. Autocorrelation between spectra was performed to reduce broadening of the peaks because of jitter or other sources of drift. The elastic peak was recorded with a 0.02-s integration time, so that the detector was never saturated and noisy but recognizable spectral features in the inelastic region could be recorded simultaneously. We subsequently energy-aligned spectra by correlating features and scaled the spectra to match at a convenient reference point, usually the first minimum above the elastic peak. (Note that the monochromator increased the

signal-to-background ratio for both the elastic and inelastic signal).

We used a commercial C_{60} crystal transferred onto a 3-mm Cu grid covered with holey carbon film. The sample was placed in a liquid-nitrogen-cooled sample holder and temperature stabilized at 130 K. Special care was taken to limit sampling to regions above holes in the carbon film so that the signal was due only to the sample itself. A rough estimate of the sample thickness was obtained from the high-angle annular dark field (HAADF) intensity scattered from the sample. This was compared to the intensity scattered from an amorphous carbon film of known thickness (5 nm). In HAADF mode the intensity is approximately proportional to $I_0 n Z^{1.7}$, where Z is the atomic number and n the number of irradiated atoms [49]. With this procedure, the thickness was estimated to be 10–15 nm. At 80-keV beam energy and a 3.3 mrad half-angle of acceptance, momentum-transfer values were up to 0.49 Å^{-1} and in all directions perpendicular to the sample normal, which was a (111) direction.

IV. RESULTS AND DISCUSSION

Figure 1 shows calculated and measured C 1s near-edge spectra. The theoretical results include a convolution with the low-loss function to simulate the experimental baselines around 300 eV. Leading peaks can be attributed to molecular orbitals and are modified slightly in the solid. The calculated first peak at 283 eV, while of approximately correct relative intensity for the BSE and StoBe calculations, is too weak in the XCH calculation, perhaps because of state-dependent screening, wherein the presence of the excited electron in a low-lying bound state could particularly lessen the screening by other electrons. Such state-dependent screening effects could depend on the inclusion of more sophisticated vertex corrections, such as those responsible for interference between extrinsic and intrinsic losses in near-threshold core-level absorption and photoemission spectra [50–53]. The second and third peaks at 283.9 eV and 284.5 eV are resolved and appear with approximately the correct relative strength for the BSE results, but with incorrect relative strength for the other two methods. These features are sensitive to details of many-body corrections to the band structure and core-hole screening. Successive higher-lying features gradually lose distinctness because of broadening effects.

Figure 2 shows the valence loss function, as measured in this work, as reported by Yagi *et al.* [19] based on visible and ultraviolet photoabsorption spectra, and as calculated. The units are absolute for the calculated loss function and that of Yagi *et al.*, whereas our measured spectrum was normalized by sight. Because of the limited energy range and uncertainty regarding multiple scattering, normalization by use of the f-sum rule did not appear to be feasible. The loss function was also reported earlier by Sohmen *et al.* [54,55]. The energy range in Fig. 2 captures most of the valence oscillator strength. Of the first four peaks predicted and measured at 2.3, 3.8, 4.9, and 5.6 eV [56–65], the highest peak is predicted to be stronger than measured but agrees with previous calculations [66]. The maximum of the loss function is predicted to be at a higher energy than either the EELS or absorption spectroscopy
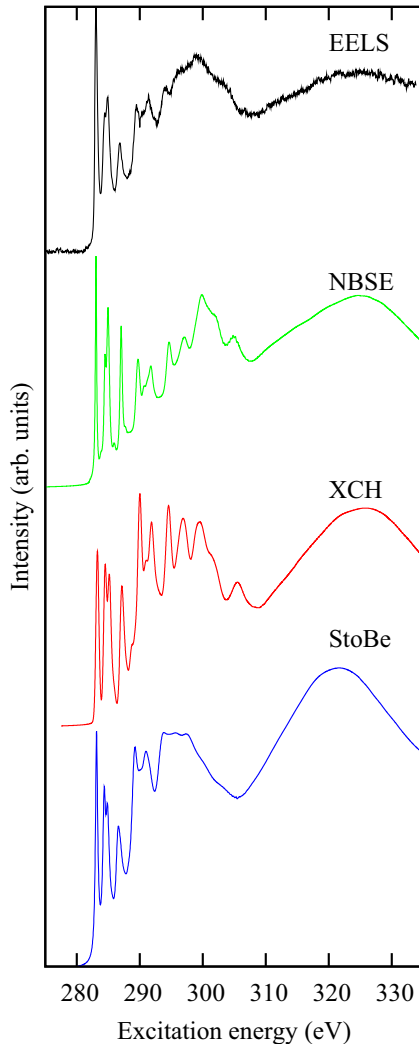

FIG. 1. C 1s near-edge spectrum as measured in this work (black curve, EELS) and calculated according to the Bethe-Salpeter equation (green curve, NIST BSE), the final-state XCH code (red curve XCH), and the transition-state STOBE code (blue curve, StoBe).
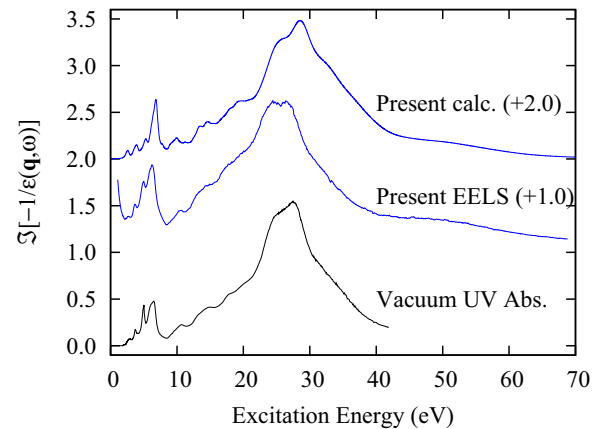

FIG. 2. Loss function based on valence BSE calculations (top), the present EELS measurements (middle), and as measured by Yagi *et al.* [19] (bottom).
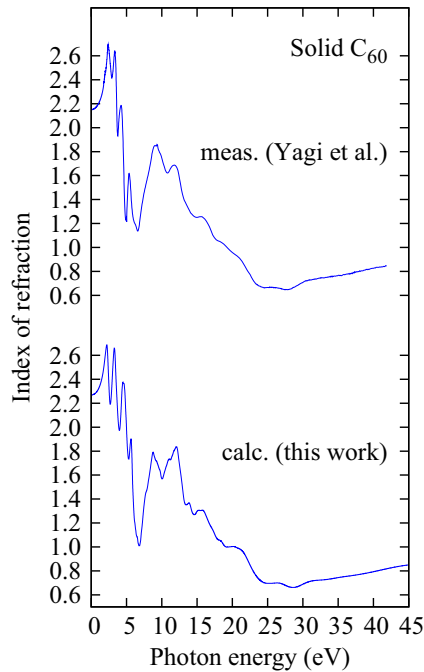
FIG. 3. Index of refraction based on valence BSE calculations and as measured by Yagi *et al.* [19].

FIG. 4. Index of absorption from valence BSE calculations and as measured by Yagi *et al.* [19].

suggest. We also note that multielectron excitation effects appear to be quite significant, judging from the loss of resolution of features above about 30 eV, just as related effects are significant in photoemission and give rise to features beyond quasiparticle peaks [51]. The theoretical reproduction of fine structure is particularly appealing when comparing the indices of refraction and absorption as in Figs. 3 and 4.

Several minor approximations that we also make should be noted. All theoretical calculations are summed over atomic sites and averaged over electric-field direction within the optical limit. The range of momentum transfer in the present measurements has a small effect in the valence loss region and an even smaller effect in the C 1*s* near-edge region. This was shown, for instance, in an earlier study of the momentum-transfer dependence of the EELS spectrum by Sohmen *et al.* [54]. However, it can play an important role in angle-resolved EELS and photoemission [67–69]. Our BSE calculations assume the *Fm*3 crystal structure. At ambient conditions there is molecular orientational disorder and the system has a 240-atom unit-cell *Pa*3 structure below 260 K [70]. Preliminary calculations and measurements only show slight changes in spectra with such structural changes. Further examination of temperature and/or orientational effects would also be of interest, but the above simplifications should have little impact. Core-hole screening in the BSE calculations was performed for each carbon site. However, only spherically symmetrical parts of the screened potentials were retained, despite anisotropic site environments. To estimate effects of the largest, quadrupolar correction to the screened core-hole potential on results, we studied this in graphite and at the boron site in hexagonal BN. This indicates that the strengths of spectral features are changed on the few-percent level.
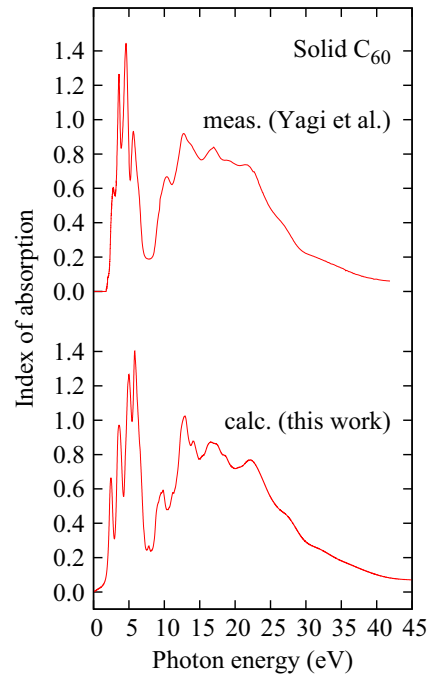
V. CONCLUSIONS

We have calculated the C 1*s* near-edge spectrum of C_{60} using the BSE approach, the final-state XCH method, and the transition-state STOBE code. The valence spectrum was additionally calculated with the BSE. Good agreement between theory and experiment is observed for the leading spectral features, while strengths of features in the theoretical spectra vary more at higher energies. The StoBe results lose most detail at energies corresponding to what would be the vacuum continuum for the free C_{60} molecule, whereas the overall, average distribution of spectral weight is approximately correct, aided by use of a sufficient basis set. Theoretical results can be quite sensitive to details of the calculation, including the strength of the electron core-hole interaction and many-body corrections to DFT band structures. For better agreement with experiment at energies several electronvolts above the onset of absorption, it is also important to include lifetime and Debye-Waller broadening and to account for transfer of spectral weight to satellites. It is encouraging that the present attempts to include these effects improve the comparisons with experiment substantially.

[1] H. W. Kroto, J. R. Heath, S. C. O'Brien, R. F. Curl, and R. E. Smalley, Nature (London) **318**, 162 (1985).

[2] W. Krätschmer, L. D. Lamb, K. Fostiropoulos, and D. R. Huffman, Nature (London) **347**, 354 (1990).

[3] J. L. Segura, N. Martín, and D. M. Guldi, Chem. Soc. Rev. **34**, 31 (2005).

[4] J. Roncali, Chem. Soc. Rev. **34**, 483 (2005).

[5] Y. Wang and L. T. Cheng, J. Phys. Chem. **96**, 1530 (1992).

[6] A. F. Hebard, M. J. Rosseinsky, R. C. Haddon, D. W. Murphy, S. H. Glarum, T. T. M. Palstra, A. P. Ramirez, and A. R. Kortan, Nature (London) **350**, 600 (1991).

[7] R. M. Fleming, A. P. Ramirez, M. J. Rosseinsky, D. W. Murphy, R. C. Haddon, S. M. Zahurak, and A. V. Makhija, Nature (London) **352**, 787 (1991).

[8] Y. Zhao, Y.-H. Kim, A. C. Dillon, M. J. Heben, and S. B. Zhang, Phys. Rev. Lett. **94**, 155504 (2005).

[9] J. J. Rehr, J. J. Kas, F. D. Vila, M. P. Prange, and K. Jorissen, Phys. Chem. Chem. Phys. **12**, 5503 (2010).

[10] P. Giannozzi and S. Baroni, J. Chem. Phys. **100**, 8537 (1994).

[11] J. Vinson, J. J. Rehr, J. J. Kas, and E. L. Shirley, Phys. Rev. B **83**, 115106 (2011).

[12] K. Gilmore, J. Vinson, E. Shirley, D. Prendergast, C. Pemmaraju, J. Kas, F. Vila, and J. Rehr, Comput. Phys. Commun. **197**, 109 (2015).

[13] E. L. Shirley, L. J. Terminello, J. E. Klepeis, and F. J. Himpsel, Phys. Rev. B **53**, 10296 (1996).

[14] D. Vanderbilt, Phys. Rev. B **32**, 8412 (1985).

[15] D. Prendergast and S. G. Louie, Phys. Rev. B **80**, 235126 (2009).

[16] E. L. Shirley, Phys. Rev. B **54**, 16464 (1996).

[17] E. L. Shirley, J. Electron Spectrosc. Relat. Phenom. **136**, 77 (2004).

[18] E. L. Shirley, Ultramicroscopy **106**, 986 (2006).

[19] H. Yagi, K. Nakajima, K. Koswattage, K. Nakagawa, C. Huang, M. Prodhan, B. Kafle, H. Katayanagi, and K. Mitsuke, Carbon **47**, 1152 (2009).

[20] P. Hohenberg and W. Kohn, Phys. Rev. **136**, B864 (1964).

[21] W. Kohn and L. J. Sham, Phys. Rev. **140**, A1133 (1965).

[22] D. M. Ceperley and B. J. Alder, Phys. Rev. Lett. **45**, 566 (1980).

[23] J. P. Perdew and A. Zunger, Phys. Rev. B **23**, 5048 (1981).

[24] E. L. Shirley and S. G. Louie, Phys. Rev. Lett. **71**, 133 (1993).

[25] N. Troullier and J. L. Martins, Phys. Rev. B **46**, 1754 (1992).

[26] L. Hedin and S. Lundqvist, in *Solid State Physics* (Elsevier BV, Amsterdam, 1970), pp. 1–181.

[27] R. W. Lof, M. A. van Veenendaal, B. Koopmans, H. T. Jonkman, and G. A. Sawatzky, Phys. Rev. Lett. **68**, 3924 (1992).

[28] R. Schwedhelm, L. Kipp, A. Dallmeyer, and M. Skibowski, Phys. Rev. B **58**, 13176 (1998).

[29] P. J. Benning, J. L. Martins, J. H. Weaver, L. P. F. Chibante, and R. E. Smalley, Science **252**, 1417 (1991).

[30] J.-M. Themlin, S. Bouzidi, F. Coletti, J.-M. Debever, G. Gensterbaum, P. Thiry, and J.-J. Pireaux, Appl. Surf. Sci. **65-66**, 76 (1993).

[31] G. Gensterblum, J.-J. Pireaux, P. A. Thiry, R. Caudano, T. Buslaps, R. L. Johnson, G. LeLay, V. Aristov, R. Günther, A. Taleb-Ibrahimi, G. Indlekofer, and Y. Petroff, Phys. Rev. B **48**, 14756 (1993).

[32] C. Heske, R. Treusch, F. J. Himpsel, S. Kakar, L. J. Terminello, H. J. Weyer, and E. L. Shirley, Phys. Rev. B **59**, 4680 (1999).

[33] M. S. Hybertsen and S. G. Louie, Phys. Rev. Lett. **55**, 1418 (1985).

[34] M. S. Hybertsen and S. G. Louie, Phys. Rev. B **34**, 5390 (1986).

[35] E. L. Shirley, Phys. Rev. B **58**, 9579 (1998).

[36] H. M. Lawler, J. J. Rehr, F. Vila, S. D. Dalosto, E. L. Shirley, and Z. H. Levine, Phys. Rev. B **78**, 205108 (2008).

[37] P. Koval, M. P. Ljungberg, D. Foerster, and D. Sánchez-Portal, Nucl. Instrum. Methods Phys. Res., Sect. B **354**, 216 (2015).

[38] D. Prendergast and G. Galli, Phys. Rev. Lett. **96**, 215502 (2006).

[39] P. Giannozzi, S. Baroni, N. Bonini, M. Calandra, R. Car, C. Cavazzoni, D. Ceresoli, G. L. Chiarotti, M. Cococcioni, I. Dabo *et al.*, J. Phys.: Condens. Matter **21**, 395502 (2009).

[40] L. Triguero, L. G. M. Pettersson, and H. Ågren, J. Phys. Chem. A **102**, 10599 (1998).

[41] K. Hermann, L. G. M. Pettersson, M. E. Casida, C. Daul, A. Goursot, A. Koester, E. Proynov, A. St-Amant, and D. R. Salahub; Contributing authors: V. Carravetta, H. Duarte, C. Friedrich, N. Godbout, J. Guan, C. Jamorski, M. Leboeuf, M. Leetmaa, M. Nyberg, S. Patchkovskii, L. Pedocchi, F. Sim, L. Triguero, and A. Vela, STOBE-DEMON version 3.1 (2011).

[42] W. Kutzelnigg, U. Fleischer, and M. Schindler, *Deuterium and Shift Calculation*, NMR: Basic Principles and Progress, Vol. 23 (Springer, Berlin Heidelberg, 1991), p. 165.

[43] A. D. Becke, Phys. Rev. A **38**, 3098 (1988).

[44] T. T. Fister, M. Schmidt, P. Fenter, C. S. Johnson, M. D. Slater, M. K. Y. Chan, and E. L. Shirley, J. Chem. Phys. **135**, 224513 (2011).

[45] J. J. Kas, A. P. Sorini, M. P. Prange, L. W. Cambell, J. A. Soininen, and J. J. Rehr, Phys. Rev. B **76**, 195116 (2007).

[46] J. J. Rehr and R. C. Albers, Rev. Mod. Phys. **72**, 621 (2000).

[47] F. Leclercq, P. Damay, M. Foukani, P. Chieux, M. C. Bellissent-Funel, A. Rassat, and C. Fabre, Phys. Rev. B **48**, 2748 (1993).

[48] R. F. Egerton, *Electron Energy-Loss Spectroscopy in the Electron Microscope* (Springer Nature, London, 1995).

[49] M. M. Treacy, Microsc. Microanal. **17**, 847 (2011).

[50] L. Campbell, L. Hedin, J. J. Rehr, and W. Bardyszewski, Phys. Rev. B **65**, 064107 (2002).

[51] J. J. Kas, J. J. Rehr, and J. B. Curtis, Phys. Rev. B **94**, 035156 (2016).

[52] M. Guzzo, G. Lani, F. Sottile, P. Romaniello, M. Gatti, J. J. Kas, J. J. Rehr, M. G. Silly, F. Sirotti, and L. Reining, Phys. Rev. Lett. **107**, 166401 (2011).

[53] L. Hedin, J. Phys.: Condens. Matter **11**, R489 (1999).

[54] E. Sohmen, J. Fink, and W. Krätschmer, Z. Phys. B: Condensed Matter **86**, 87 (1992).

[55] E. Sohmen and J. Fink, Phys. Rev. B **47**, 14532 (1993).

[56] H. Ajie, M. M. Alvarez, S. J. Anz, R. D. Beck, F. Diederich, K. Fostiropoulos, D. R. Huffman, W. Kraetschmer, Y. Rubin *et al.*, J. Phys. Chem. **94**, 8630 (1990).

[57] T. W. Ebbesen, K. Tanigaki, and S. Kuroshima, Chem. Phys. Lett. **181**, 501 (1991).

[58] S. Leach, M. Vervloet, A. Després, E. Bréheret, J. P. Hare, T. J. Dennis, H. W. Kroto, R. Taylor, and D. R. Walton, Chem. Phys. **160**, 451 (1992).

[59] Y. Achiba, T. Nakagawa, Y. Matsui, S. Suzuki, H. Shiromaru, K. Yamauchi, K. Nishiyama, M. Kainosho, H. Hoshi, Y. Maruyama, and T. Mitani, Chem. Lett. **20**, 1233 (1991).

[60] A. Skumanich, Chem. Phys. Lett. **182**, 486 (1991).

[61] A. F. Hebard, R. C. Haddon, R. M. Fleming, and A. R. Kortan, Appl. Phys. Lett. **59**, 2109 (1991).

[62] A. L. Smith, J. Phys. B: At., Mol. Opt. Phys. **29**, 4975 (1996).

[63] H. Kataura, Y. Endo, Y. Achiba, K. Kikuchi, T. Hanyu, and S. Yamaguchi, J. Phys. Chem. Solids **58**, 1913 (1997).

[64] C. Hartmann, M. Zigone, G. Martinez, E. L. Shirley, L. X. Benedict, S. G. Louie, M. S. Fuhrer, and A. Zettl, Phys. Rev. B **52**, R5550 (1995).

[65] G. Gensterblum, J. J. Pireaux, P. A. Thiry, R. Caudano, J. P. Vigneron, P. Lambin, A. A. Lucas, and W. Krätschmer, Phys. Rev. Lett. **67**, 2171 (1991).

[66] J. Kauczor and P. Norman, J. Chem. Theory Comput. **10**, 2449 (2014).

[67] M. Schüler, J. Berakdar, and Y. Pavlyukh, Phys. Rev. A **92**, 021403 (2015).

[68] M. Schüler, Y. Pavlyukh, P. Bolognesi, L. Avaldi, and J. Berakdar, Sci. Rep. **6**, 24396 (2016).

[69] P. Bolognesi, L. Avaldi, A. Ruocco, A. Verkhovtsev, A. Korol, and A. Solov'yov, Eur. Phys. J. D **66**, 1 (2012).

[70] W. I. F. David, R. M. Ibberson, T. J. S. Dennis, J. P. Hare, and K. Prassides, Europhys. Lett. **18**, 219 (1992).